Eur. Phys. J. D **45**, 139–145 (2007)
DOI: 10.1140/epjd/e2007-00179-4

THE EUROPEAN PHYSICAL JOURNAL D

Prospects of ion-mobility measurements in superheavy element research

M. Sewtz[a], M. Laatiaoui, K. Schmid, and D. Habs

Department für Physik, Ludwig-Maximilians-Universität München, 85748 Garching, Germany

Received 22 January 2007 / Received in final form 29 March 2007
Published online 1st June 2007 – © EDP Sciences, Società Italiana di Fisica, Springer-Verlag 2007

Abstract. The element specific electron configuration of ions directly reflects the two quantum mechanical observables $\langle r^2 \rangle$ and r_{max}, which denote the r^2 expectation value of the electron density and the principle maximum of the wave function of the outermost electron orbital, respectively. Thus, the determination of these observables may present a new access to element identification of single superheavy nuclides. In this paper, we discuss how these observables are related to ionic radii deduced from ion-mobility data using the most simple hard sphere model and semi-empirical $(n, 6, 4)$ model potentials for the interaction of heavy ions with noble gases. A concept for a high resolution ion-mobility spectrometer is presented. Optimum extraction efficiency of the ions will be achieved by decoupling the ion motion from the electric field drift by the friction force of the suitably shaped gas flow at the exit nozzle.

PACS. 27.90.+b Properties of superheavy elements – 31.10.+z Theory of electronic structure, electronic transitions, and chemical binding – 51.10.+y Kinetics and transport theory of gases – 52.20.Hv Atomic, molecular, ion, and heavy-particle collisions

1 Introduction

Today's most advanced method for investigations of the properties of transfermium elements is gas phase chemistry with single atoms. This method yielded detailed chemical information up to element 108 (hassium) [1] and — most recently — first experiments at element 112 [2] were successfully performed. These investigations aim at the examination of the chemical properties within one group of homologous elements. Deviations from the periodicity in the atomic shell structure may be caused by relativistic effects which gain in particular importance for the heaviest elements in the region beyond $Z = 100$. Relativistic effects are caused, roughly speaking, by a contraction of the wave functions of s- and $p_{1/2}$-electrons. Inner shell electrons influence indirectly via the shielding of the nuclear potential the valence electrons and, thus, the chemical properties as well. The comparison with relativistic ab-initio calculations [3] happens via the adsorption enthalpy — a thermodynamic property.

However, direct comparison of the measured quantities with the quantum mechanical observables would represent a microscopic test of Dirac-Fock calculations. The radial maximum of the wavefunction of the outermost orbital, r_{max} and the expectation value $\langle r^2 \rangle$, are both not only subjected to the above mentioned relativistic contraction but also reflect the electron configuration of the respective atoms [4] and ions, see Figure 1. Thus, systematic studies of r_{max} and $\langle r^2 \rangle$ of actinides and transactinides will contribute to a better understanding of the electronic structure in strong (nuclear) fields. The contraction of neighboring actinides amounts to >1% [5] whereof 20% are caused by relativistic effects [6]. Also QED effects gain importance for the heaviest elements and cause changes in the valence electron binding energies of >0.1 eV [7] which contributes to the actinide contraction. Since atomic physics investigations of actinides

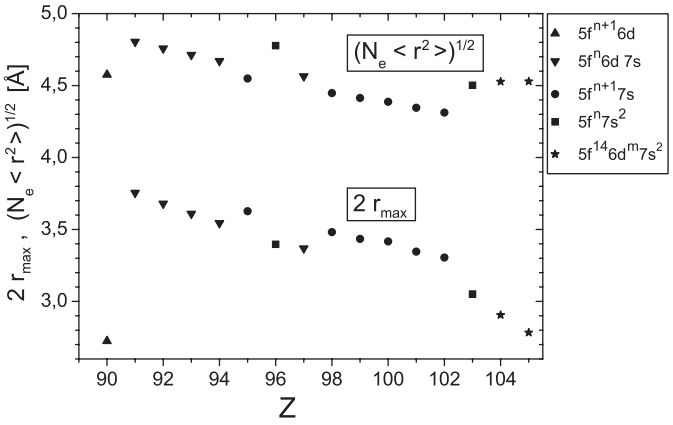

Fig. 1. Maximum of the outermost radial wave function r_{max} and $\sqrt{N_e \langle r^2 \rangle}$ as function of the charge number Z. The number of electrons in the $5f$-shell is $n = Z - 89$ and in the $6d$-shell $m = Z - 103$. Values taken from reference [5].

[a] e-mail: michael.sewtz@physik.uni-muenchen.de

and transactinides require extremely sensitive methods, no such experiments have been performed with these elements, so far.

Kemper and Bowers [8] have shown that not only electron configurations of ions can be deduced from ion-mobility measurements but that it is even possible to distinguish between metastable ionic states. The development of this technique at trace amounts of shortlived actinides [9,10] may pave the way for investigations up to the heaviest elements which may be of particular interest for the identification of the heaviest nuclides observed in "hot" fusion reactions [11]. Combining nuclear charge number Z-selective ion-mobility measurements with mass analysis may allow for definite identification of the neutron rich isotopes presently assigned to ^{267,268}Rf and ^{267,268}Db and thus for a connection of the decay chains of the heaviest elements to the well established part of the chart of nuclei.

In this paper, we discuss how the two quantum mechanical observables r_{max} and $\langle r^2\rangle$ can be deduced from ion-mobility measurements of actinides (AC) and lanthanides (LA), either directly, assuming hard sphere collisions, see Section 3, or via the determination of semi-empirical interaction potentials, see Section 4. Here, r_{max} denotes the principal maximum of the radial wave function of the outermost ionic orbital and $N_e\langle r^2\rangle$ denotes the sum of the expectation value $\langle r_i^2\rangle$ of each orbital i, $\sum_{N_e}\langle r_i^2\rangle = N_e\langle r^2\rangle$, where $N_e = Z - 1$ is the number of electrons of the respective ion. The values $\langle r^2\rangle$ are taken from reference [5]. Both quantities r_{max} and $\sqrt{N_e\langle r^2\rangle}$ directly reflect the electron configuration of the ions as shown in Figure 1. In Section 5 we present design studies for a suitable drift cell for on-line ion-mobility measurements of transactinide elements.

2 Experimental

In references [10,12] shifts were observed in the time distribution spectra of mono atomic and molecular actinide ions created by resonance ionization in a buffer gas cell. In these experiments, the ions drift inside the buffer gas cell along electric field lines and are extracted with a time delay of roughly 1 ms. From this time delay $t_d = \int_S ds/v_D(s) = \frac{1}{K}\int_S ds/E(s)$, the ion mobility K was deduced using the known integral $\int_S ds/E(s)$ along the trajectory s. Here, $v_D(s) = KE(s)$ is the instantaneous ion drift velocity at point s of the trajectory. At an argon buffer gas pressure of 100 mbar and a mean electric field strength of $\bar{E} = 25.6$ V/cm, the parameter E/N amounts to $E/N \approx 1$ Td, with the number density N of buffer gas atoms.

From the determined ion mobility K, the momentum transfer cross section Ω was calculated from the first order expression [13]

$$\Omega = \frac{3}{16}\frac{e}{n}\sqrt{\frac{2\pi}{\mu k_B T_{eff}}}\frac{1}{K}$$

neglecting the field dependence $K(E)$ which is reasonable at the low values of E/N applied in the measurements. Here, e denotes the electron charge, μ the reduced mass, and k_B the Boltzmann constant. The effective temperature T_{eff} is given by

$$\frac{3}{2}kT_{eff} = \frac{3}{2}kT + \frac{1}{2}Mv_D^2 \approx \frac{3}{2}kT$$

with M the mass of the Ar-atoms and the measured temperature $T = 80$ °C of the optical cell.

3 Description of ion-atom interaction by hard sphere collisions

In the rigid sphere model, the momentum transfer cross section can be written as

$$\Omega = \pi d^2 = \pi(r_{\mathrm{Ar}} + r_{ion})^2 \tag{1}$$

and the ionic radius r_{ion} can be deduced if the radius r_{Ar} of argon is known. Relative changes of ionic radii can be determined much more precisely from the relative drift time differences:

$$\frac{\Delta t_d^{A,B}}{t_d^B} = \frac{\sqrt{\mu^A}\Omega^A - \sqrt{\mu^B}\Omega^B}{\sqrt{\mu^B}\Omega^B}.$$

For actinides in argon, $\mu^A \approx \mu^B$ and hence

$$\frac{\Delta t_d^{A,B}}{t_d^B} \approx \frac{\Delta\Omega^{A,B}}{\Omega^B} \approx \frac{2\Delta r^{A,B}}{r_{\mathrm{Ar}} + r_B}, \tag{2}$$

with $\Delta\Omega^{A,B} = \Omega^A - \Omega^B$ and $\Delta r^{A,B} = r^A - r^B$. To apply the rigid sphere model also to observed AC-monoxide ions, the most simple Ansatz for the radius of molecules $r_M = r_{max}(\mathrm{ion}) + r_{max}(\mathrm{O})$ and $r_M = \sqrt{N_e\langle r^2\rangle}(\mathrm{ion}) + \sqrt{N_e\langle r^2\rangle}(\mathrm{O})$ was used. Changes in the relative cross sections $\Delta\Omega^{A,B}/\Omega^B$ using r_{max} or $\sqrt{N_e\langle r^2\rangle}$ in equations (1) and (2) are listed in Table 1.

4 Description of ion-atom interaction by semi-empirical potentials

Ion-atom interactions can be described as the sum of one repulsion term and two attraction terms [14],

$$V(r) = \frac{C_n}{r^n} - \frac{C_6}{r^6} - \frac{C_4}{r^4}, \tag{3}$$

where the constants n and C_n are adapted empirically to the data. At low temperatures and weak electric fields, long range interaction is dominated by dipole polarization V_p^D which defines the coefficient C_4:

$$C_4 = -V_p^D r^4 = \frac{e^2\alpha_{\mathrm{Ar}}}{2(4\pi\epsilon_0)^2}. \tag{4}$$

Table 1. Relative changes of collision cross sections $\Delta\Omega^{A,B}/\Omega^B = (\Omega^A - \Omega^B)/\Omega^B$ of mono atomic and molecular actinide ions in argon. For ionic and atomic radii (*a*) r_{max} and (*b*) $\sqrt{N_e\langle r^2\rangle}$ from Table 2 have been used.

Ion A	Ion B	Experimental values [10,12]	Rigid sphere Model (*a*)	Rigid sphere Model (*b*)	(12, 6, 4) Model	(8, 6, 4) Model Solution (*c*), Table 4	(8, 6, 4) Model Solution (*d*), Table 4
Am^+	Pu^+	−0.04(1)	0.03	−0.05	-1.3×10^{-3}	4.8×10^{-4}	1.5×10^{-4}
Fm^+	Cf^+	−0.02(1)	−0.03	−0.02	-6.4×10^{-4}	2.4×10^{-4}	7.6×10^{-5}
UO^+	Cf^+	0.20(1)	0.44	0.30	4.2×10^{-3}	-1.3×10^{-3}	-4.2×10^{-4}
PuO^+	Pu^+	0.29(1)	0.36	0.17	7.0×10^{-4}	-2.6×10^{-4}	-8.3×10^{-5}

Table 2. Maximum of the outermost radial wave function r_{max} and $\sqrt{N_e\langle r^2\rangle}$ for atoms and ions. Values taken from reference [5].

			O	Ar	U	Pu	Am	Cf	Fm
r_{max}	[Å]	(Atom)	0.44	0.69	1.95	1.98	1.95	1.86	1.80
r_{max}	[Å]	(Ion)	–	–	1.84	1.77	1.81	1.74	1,71
$\sqrt{N_e\langle r^2\rangle}$	[Å]	(Atom)	0.44	0.64	5.50	5.37	5.32	5.17	5.08
$\sqrt{N_e\langle r^2\rangle}$	[Å]	(Ion)	–	–	4.76	4.67	4.55	4.45	4.39

Table 3. Polarizabilities of atoms α_{atom} and ions α_{ion}.

	O	Ar	U	Pu	Am	Cf	Fm	UO	PuO
α_{atom} [Å^3]	0.802[a]	1.64[a]	27.4[b]	24.5[b]	23.3[b]	20.5[b]	18.9[b]	–	–
α_{ion} [Å^3]	–	–	14.8[c]	13.5[c]	12.06[c]	10.87[c]	10.24[c]	15.6[d]	14.3[d]
α^e_{atom} [Å^3]	–	–	8.37[e]	7.45[e]	7.09[e]	6.13[e]	5.57[e]	–	–
α^e_{ion} [Å^3]	–	–	4.53[e]	4.12[e]	3.67[e]	3.25[e]	3.02[e]	–	–
N_{atom}	–	5.52[a]	3[g]	3[g]	3[g]	3[g]	3[g]	–	–
N_{ion}	–	–	2[g]	2[g]	2[g]	2[g]	2[g]	2[g]	2[g]

[a] Taken from reference [13]. [b] Calculated polarizabilities taken from reference [19].
[c] Derived from equation (7). [d] Derived from equation (8).
[e] Derived from equation (6). [g] From comparison with lanthanides, see Section 4.

Here, ϵ_0 denotes the dielectric constant. With $e^2/(4\pi\epsilon_0)^2 = 14.4$ eV Å and the polarizability of argon $\alpha_{\mathrm{Ar}} = 1.642$ Å^3 [13] we get $C_4 = 11.81$ eV Å^4.

The inverse sixth power term describes the interaction based on permanent dipoles or higher multipoles of one partner which induce multipole moments on the other [15], charge induced quadrupole moments, and the lowest order term of the dispersion interaction V_{dis} [16]. Considering mono-atomic ions in noble gases, the first contribution results in zero. The contribution of the charge induced quadrupole polarization energy V_q compared to the dipole-dipole dispersion energy V_{dis} can be estimated for heavy alkalies in argon from reference [16] to be $V_q/V_{dis} \approx 0.26$ and is thus neglected in the following:

$$C_6 \approx -V_{dis}r^6 = \frac{3}{2}\frac{\alpha_{ion}\alpha_{\mathrm{Ar}}}{\sqrt{\alpha_{ion}/N_{ion}} + \sqrt{\alpha_{\mathrm{Ar}}/N_{\mathrm{Ar}}}}. \quad (5)$$

The equivalent oscillator number of argon amounts to $N_{\mathrm{Ar}} = 5.52$ [17] and of ytterbium atoms to $N_{\mathrm{Yb}} \approx 3$ [18] yielding $N_{ion} \approx 2$ for Yb^+ ions. Since the equivalent oscillator numbers of Tm and Yb are similar [18], we assume that there are no big changes in the heavy lanthanides and actinides and hence $N_{AC^+} \approx 2$. The calculated atomic polarizabilities [19] of the actinides are listed in Table 3. Obviously a wrong ground state configuration for fermium has been assumed in reference [19], therefore $\alpha_{\mathrm{Fm}} = 18.9$ Å^3 has been interpolated. The unknown polarizabilities of actinide ions can be estimated from the formula [20]

$$\alpha^e = \frac{4}{9N_e a_0}\left(\sum_{i=1}^{N_e}\langle r_i^2\rangle\right)^2, \quad (6)$$

where N_e is the number of electrons in the atom, a_0, the Bohr atomic radius, and $\langle r_i^2\rangle$ the mean square distance of the ith electron from the nucleus. The sum $\sum_{i=1}^{N_e}\langle r_i^2\rangle = N_e\langle r^2\rangle$ can be evaluated using listed values of $\sqrt{N_e\langle r^2\rangle}$ for atoms and ions from Table 2. Equation (6) yields precise values only for nobel gas configurations, compare with reference [16]. Therefore, equation (6) is only taken to calculate the ratio of the polarizabilities of ions and atoms:

$$\alpha_{ion} = \alpha_{atom}\frac{\alpha^e_{ion}}{\alpha^e_{atom}}. \quad (7)$$

A good estimate for the polarizability of simple molecules is the sum of the polarizability of the constituents [16]

$$\alpha_{molecule^+} = \alpha_{ion} + \alpha_{atom} \quad (8)$$

where α_{ion} is the polarizability of AC^+ and α_{atom} the polarizability of oxygen. All deduced polarizabilities are listed in Table 3.

Table 4. Parameters for $(n, 6, 4)$ potentials with $n = 12$ and $n = 8$ calculated from equation (5) and equations (9–12). (a) From comparison with Tl^+ in Ar, see Section 4. (b) Interpolated from reference [14]. $(c), (d)$ Real solutions of equation (12) with $\gamma \leq 1$.

	U	Pu	Am	Cf	Fm	UO	PuO
C_4 [eV Å^4]	11.81	11.81	11.81	11.81	11.81	11.81	11.81
C_6 [eV Å^6]	6.65	6.30	5.90	5.55	5.35	6.86	6.52
ε [eV] (a)	0.11	0.11	0.11	0.11	0.11	0.11	0.11
$T^\star$	0.3	0.3	0.3	0.3	0.3	0.3	0.3
$n = 12$							
γ [10^{-3}]	7.7	7.3	6.9	6.5	6.3	7.9	7.6
r_m [Å]	2.943	2.942	2.940	2.938	2.937	2.945	2.943
$\Omega^\star(\gamma, T^\star)$ (b)	2.709	2.709	2.709	2.709	2.710	2.709	2.709
$n = 8$ (c)							
γ [10^{-2}]	4.6	4.3	4.1	3.8	3.7	4.7	4.5
r_m [Å]	2.181	2.181	2.181	2.181	2.181	2.181	2.181
$\Omega^\star(\gamma, T^\star)$ (b)	2.983	2.984	2.985	2.986	2.987	2.982	2.983
$n = 8$ (d)							
γ [10^{-2}]	1.2	1.2	1.1	1.0	1.0	1.3	1.2
r_m [Å]	2.716	2.716	2.716	2.717	2.717	2.716	2.716
$\Omega^\star(\gamma, T^\star)$ (b)	2.998	2.998	2.999	2.999	2.999	2.998	2.998

It is convenient to write equation (3) in dimensionless form

$$V(r) = \frac{n\varepsilon}{n(3+\gamma) - 12(1+\gamma)} \times \left[\frac{12}{n}(1+\gamma)\left(\frac{r_m}{r}\right)^n - 4\gamma\left(\frac{r_m}{r}\right)^6 - 3(1-\gamma)\left(\frac{r_m}{r}^4\right)\right]$$

with three parameters: the depth of the potential minimum ε at the ion-atom distance r_m and γ, the relative strength of the repulsive $1/r^n$ term.

The parameters γ and r_m can be evaluated by comparison of coefficients for $n = 12$:

$$\gamma = \frac{C_6}{2\varepsilon r_m^6} \tag{9}$$

$$C_4 = \frac{3}{2}\varepsilon(1-\gamma)r_m^4 \Rightarrow r_m^6 - \frac{2}{3}\frac{C_4}{\varepsilon}r_m^2 - \frac{1}{2}\frac{C_6}{\varepsilon} = 0 \tag{10}$$

and $n = 8$:

$$\gamma = \sqrt{1 + \frac{C_6}{6\varepsilon r_m^6}} - 1 \approx \frac{C_6}{12\varepsilon r_m^6} \quad (\text{for } \gamma \ll 1) \tag{11}$$

$$C_4 = 2\varepsilon\frac{3(1-\gamma)}{3-\gamma}r_m^4 \Rightarrow r_m^{14} - \frac{23}{35}\frac{C_4}{\varepsilon}r_m^{10} + \frac{3}{28}\frac{{C_4}^2}{\varepsilon^2}r_m^6 + \frac{1}{210}\frac{C_4C_6}{\varepsilon^2}r_m^4 - \frac{1}{840}\frac{C_6{C_4}^2}{\varepsilon^3} = 0. \tag{12}$$

The depth $\varepsilon = 0.11$ eV of the interaction potential can be estimated from the interaction of Tl^+ in Ar [21]. If dipole polarization is the dominant term at r_m, ε is equal for all ions in the same gas, see equation (4). Calculated parameters C_4, C_6, γ, and r_m are listed in Table 4. The collision integrals $\Omega = \Omega^\star \pi r_m^2$ are derived from tabulated values for $\Omega^\star$ from reference [14]. The thermal energy amounts to $3kT/2 = 0.046$ eV at a buffer gas temperature of 80 °C, hence $T^\star = kT/\varepsilon = 0.3$. Relative changes in the cross sections $\Delta\Omega^{A,B}/\Omega^B$ are listed in Table 1.

5 Experimental set-up for high-precision ion-mobility measurements of single ions

Drift time spectrometers typically allow for wide variations of E/N by changing the buffer gas pressure and the electric field E, see reference [13] and references therein. The parameter E/N determines the kinetic energy of the ions. Thus, its variation allows for probing the different $1/r^n$ terms in equation (3) with $n = 4, 6, 8, 12, ...$ Considering ion-mobility measurements for the assignment of A and Z of single, superheavy ions, extended measurements at different E/N may be hampered by the low production rates of <1/min. Hence, it is envisaged to determine Z via the measurement of $\langle r^2 \rangle$ or r_{max}, see Section 6, at one fixed value $E/N \approx 1$ Td using an ultra-sensitive set-up similar to that described in references [10,12].

However, nuclear fusion reactions are necessary for the production of transfermium elements. Therefore, experiments are planned at the UNILAC accelerator facility of GSI in Darmstadt behind the recoil separators SHIP [22] and TASCA [23] which will allow for suppression of background from scattered primary beam particles and transfer products to <100/s. After passing a thin entrance foil, the fusion reaction products will be stopped directly in the drift time spectrometer which consists of 21 ring electrodes and has a total length of 35 cm, see Figure 2. The ring electrodes at the beginning of the drift path have an inner diameter of 90 mm, which is necessary to contain the stopping volume of the recoil ions in the buffer gas cell. The stopping volume amounts, e.g., for Yb^+ ions produced in the nuclear fusion reaction ^{107}Ag(^{52}Cr,

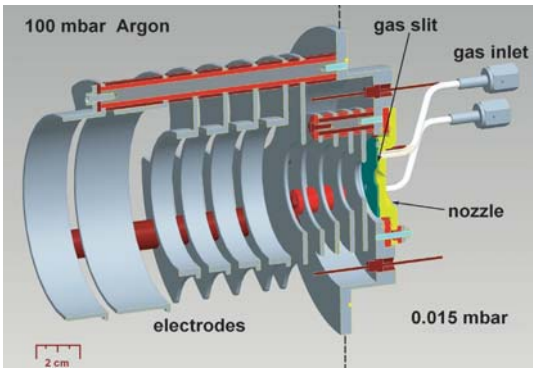

Fig. 2. (Color online) Cross section plot of the ion-mobility spectrometer for superheavy elements. Only the extraction part is shown. The spacing between electrodes amounts to 5 mm.

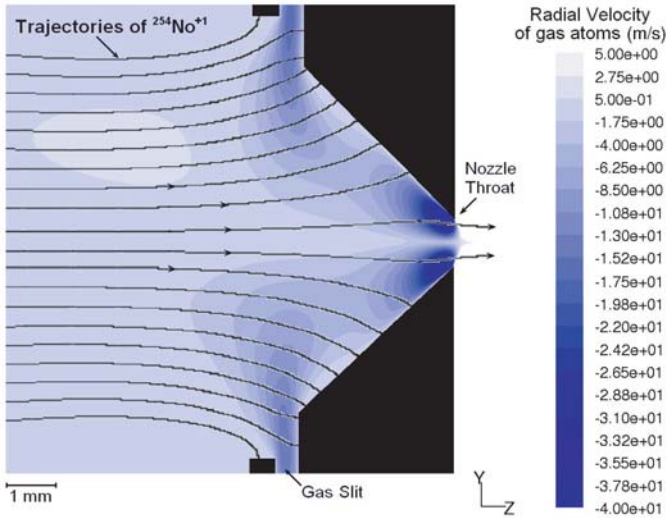

Fig. 3. Contour plot of the radial velocities of argon buffer-gas atoms at a gas flow rate of 14 mbar l/s at the nozzle. Negative velocities indicate focussing versus the axis of symmetry. Trajectories of $^{254}No^{+1}$ ions are shown to demonstrate the defocusing effect resulting from the electrostatic guiding field without considering the gas flow.

$p3n)^{155}$Yb at SHIP, to about 10^2 cm^3 having the lateral extension $\sigma_x \approx 23$ mm at an argon buffer gas pressure of 100 mbar [24]. The extraction side of the electrode system is characterized by a decreasing inner diameter of the electrodes for focusing of the ions through an exit nozzle with a throat of $d = 1$ mm diameter. Three gas inlets are foreseen to achieve a homogeneous gas flow at the nozzle cone, see Figure 3. The required argon pressure for the stopping of the recoiling fusion products limits the parameter E/N to about 1 Td and results in a gas flow rate of about 14 mbar l/s through the nozzle, which creates a background pressure in the adjacent vacuum chamber of 1.5×10^{-2} mbar. The rear part of the set-up consists of a differential pumping section and mass selective ion detection similar to the set-up described in reference [9].

Optimization of the drift cell

The electrode system which is shown in Figure 2 has been optimized for ion-mobility measurements with a resolution of $\delta K/K < 1\%$ necessary for the observation of changes in the ionic radii, see Section 3. Electric fields and ion trajectories were calculated using the computer code SIMION [25] and are shown in Figure 4. To minimize the drift time differences caused by different lateral starting points of the ions, the potentials are chosen such, that the ions drift in a homogenous electric field of about 25 V/cm before they are focused towards the axis of symmetry only about 50 mm in front of the nozzle. The resulting relative difference in the drift time amounts to $\Delta t_d/t_d < 10^{-3}$ for a given longitudinal starting position z.

Two different potential configurations are shown in Table 5. By using configuration (a), the ions are purely focused by the steadily increasing electric field gradient. Due to the non-vanishing width, $w = 3$ mm, of the conducting nozzle at the potential U_1, all ions are guided onto this electrode if they arrive at a distance $r \geq d/2$ from the axis of symmetry, see Figure 4a. This is the dominant fraction of the ions transported from the stopping region centered at $z \approx 40$ mm even though the maximum field gradient is set between the nozzle and the first electrode leading

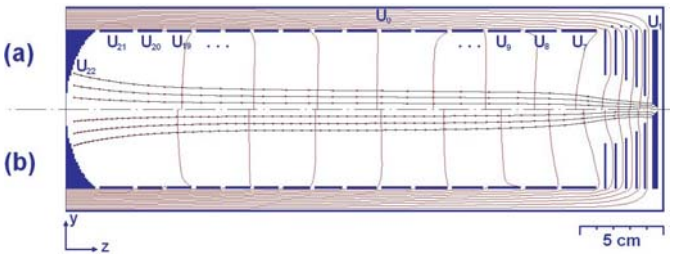

Fig. 4. Simulation of electrical fields and $^{254}No^{+1}$ ion trajectories from $z = 0$ mm towards the nozzle in 100 mbar Ar. (a) Strong and (b) moderate electrostatic field focussing using the electrode potentials listed in Table 5. Time stamps with $\Delta t = 1$ ms are indicated on each trajectory.

to $E \approx E_{crit}$ with the critical field for voltage breakdown $E_{crit} = 1.1$ kV/cm [26]. The strong focusing results in the high radial velocity $v_{rad} \approx 27$ m/s of the ions hitting the nozzle. In reference [27], it has been proposed to slow down the ions in front of the nozzle so that the gas flow becomes the dominating effect which would in turn lead to further electrostatic defocusing. A similar idea was followed in configuration (b), which represents a combination of electrostatic and gas-flow focusing, see Figures 4b and 3. The electric field gradient steadily increases from U_{21} to U_2 and decreases between the first electrode and the nozzle which reduces the radial velocity of the ions hitting the nozzle to about $v_{rad} \approx 10$ m/s. In this case, the electrostatic forces can be counteracted by the friction force of the gas flow. However, reducing the electric potentials as listed in Table 5 results in an increase of the drift time from 25 ms (a) to 60 ms (b). Envisaging experiments with short-lived nuclides, the drift time should not exceed 100 ms.

Table 5. HV-potentials used in the electric field calculations, see Figure 4. The potential decreases from U_{21} to U_{10} in steps of 125 V (a) and 50 V (b) resulting in a homogenous electric drift field of 60 V/cm and 25 V/cm, respectively.

	U_{22}[V]	U_{21}[V]	...	U_{10}[V]	U_9[V]	U_8[V]	U_7[V]	U_6[V]	U_5[V]	U_4[V]	U_3[V]	U_2[V]	U_1[V]	U_0[V]
(a)	3520	3480	...	2110	1930	1750	1570	1370	1160	940	700	420	20	0
(b)	1500	1480	...	930	860	790	710	610	510	400	270	130	40	0

In this paper, we present a gas inlet system, see Figure 2, which uses the gas flow of the argon buffer gas for additional focusing of the ions. The gas provided from three gas inlets passes a 0.5 mm wide slit which is part of the nozzle and causes a homogenous gas flow into the nozzle throat. Figure 3 shows a contour plot of the radial gas velocities at the nozzle obtained from the computer code for gas-dynamic simulations FLUENT 6.2 [28]. According to the simulations, radial gas velocities >10 m/s with a focusing effect for the ions are achieved at the gas inlet. The closer the ions drift towards the nozzle throat, the stronger becomes the gas focusing mechanism. At the nozzle throat, the friction force in the emerging buffer gas jet dominates the ion motion and the ions are extracted out of the buffer gas cell.

Without further knowledge of the starting position z, the resolution will be limited by the ratio of the width of the stopping distribution to the length of the drift path to $\delta K/K \approx 0.07$. Therefore, it is planned to deduce relative differences of the radii of superheavy and argon ions from relative drift time measurements, see equation (2). Argon atoms are ionized during the slowing down of the fusion products and can be registered prior to the superheavy ion itself.

6 Conclusion

The element-specific electron configuration of ions directly reflects the two quantum mechanical observables $\langle r^2 \rangle$ and r_{max}, see Figure 1, which opens up a new access to element identification of the heaviest nuclides. However, electron configuration changes may hamper unambiguous distinction between, e.g., Am ($Z = 95$) and Np ($Z = 93$) considering $\langle r^2 \rangle$, or Cm ($Z = 96$) and U ($Z = 92$) considering r_{max}. Nevertheless, the determination of $\langle r^2 \rangle$ or r_{max} in combination with mass number A analysis, i.e., determination of the mass of the ions with $\Delta m/m \leq 1/A \approx 1/300$ which is feasible with commercial quadrupole mass filters, will present severe constraints for the assignment of most actinides and transactinides.

In Table 1, measured collision cross section ratios for different actinide ions in argon from references [10,12] are compared with the respective ratios calculated using the hard sphere model, see Section 3, and (n, 6, 4) model potentials with $n = 12$ and $n = 8$ as discussed in Section 4.

We find good agreement between the deduced collision cross section ratios using $\langle r^2 \rangle$ and r_{max} as ionic radii in the most simple hard sphere model, see Section 3, and the experimental data. The opposite trends of r_{max} and $\sqrt{N_e \langle r^2 \rangle}$ between Pu and Am, may be a hint that ion mobility is rather sensitive to $\sqrt{N_e \langle r^2 \rangle}$ than to r_{max}. This finding calls for systematic investigations using the refined experimental set-up described in Section 5.

Both semi-empirical model potentials discussed in Section 4 fail to explain the observed shrinking of the cross sections of mono atomic actinide ions with increasing charge number Z if we assume that ε does not vary in the actinides.

Even more obvious is the discrepancy in the cross section ratios of mono atomic and molecular ions of ≥20%, see Table 1. Using these models, long range forces, i.e., ion-dipole interaction — which is independent of the atomic structure of the ion — dominates the ion-atom interaction at zero-temperature ($kT \ll \varepsilon$).

Thus, the observed differences in collision cross sections for different actinide ions can only be accounted for if we assume small variations in the potential depth ε, note that Ω is proportional to $\sqrt{\varepsilon}$ [14]. This parameter can only be determined, if the absolute collision cross section Ω can be measured with sufficient precision of $\delta\Omega/\Omega < 0.01$ which was not possible with the set-up used in references [10,12]. Therefore, a suitable drift time spectrometer for rare radioactive ions is being constructed, see Section 5. Another Ansatz is the determination of Ω at different values of E/N. Detailed studies of the mobility of O^+ ions in argon [29] have shown perfect agreement with quantum chemical calculations [30].

Using the (n, 6, 4) models, all atomic structure information about the ions is hidden in ε. All actinide ions apart from Th, Cm, and Lr have a $5f^{n+1}7s$ or $5f^n6d7s$ configuration. In reference [18], the authors have shown, that the $5f$ electrons are so well shielded by the $7s^2$ valence electrons of actinide atoms, that their contribution in collisions is negligible. If this is also true for the ions, the interaction is dominated by the contribution of the $7s$ valence orbital which is subjected to the actinide contraction, see Figure 1. Note that the maxima of the outermost radial wave functions r_{max} of Ar ($r_{max} = 0.7$ Å [4]) and of AC^+ ($r_{max} \approx 1.9$ Å [5]) overlap at the mean value of the calculated minima $r_m \approx 2.6$ Åof the Ar-AC^+ interaction potentials, see Tables 2 and 4. Here, detailed quantum chemical calculations are needed to deduce the influence of the size of the $7s$ orbital on the potential depth ε.

Fruitful discussions with P. Indelicato, H. Backe, W. Lauth, and P. Kunz are gratefully acknowledged. Further, we would like to thank L.A. Viehland for his instructive comments and critical remarks.

References

1. C. Düllmann et al., Nature **418**, 859 (2002)
2. R. Eichler, N.V. Aksenov, A.V. Belozerov, G.A. Bozhikov, V.I. Chepigin, S.N. Dmitriev, R. Dressler, H.W. Gäggeler, V.A. Gorshkov, F. Haenssler, M.G. Itkis, A. Laube, V.Ya. Lebedev, O.N. Malyshev, Yu.Ts. Oganessian, O.V. Petrushkin, D. Piguet, P. Rasmussen, S.V. Shishkin, A.V. Shutov, A.I. Svirikhin, E.E. Tereshatov, G.K. Vostokin, M. Wegrzecki, A.V. Yeremin, Nature **447**, 72 (2007)
3. V. Pershina, Chem. Rev. **96**, 1977 (1996)
4. J. Desclaux, At. Data Nucl. Data Tables **12**, 311 (1973)
5. P. Indelicato, J.P. Santos, S. Boucard, J.P. Desclaux, Eur. Phys. J. D **45**, 155 (2007)
6. P. Pyykkö, Chem. Rev. **88**, 563 (1988)
7. P. Pyykkö, M. Tokman, L. Labzowsky, Phys. Rev. A **57**, R689 (1998)
8. P. Kemper, M. Bowers, J. Am. Chem. Soc. **112**, 3231 (1990)
9. M. Sewtz et al., Phys. Rev. Lett. **90**, 163002 (2003)
10. M. Sewtz et al., Spectrochim. Acta B **58**, 1077 (2003)
11. Yu.Ts. Oganessian, Eur. Phys. J. D **45**, 17 (2007)
12. H. Backe, A. Dretzke, R. Horn, T. Kolb, W. Lauth, R. Repnow, M. Sewtz, N. Trautmann, Hyp. Int. **162**, 77 (2005)
13. E. Mason, E. McDaniel, *Transport Properties of Ions in Gases* (John Wiley & Sons, New York, Chichester, Brisbane, Toronto, Singapore, 1988)
14. L. Viehland, E. Mason, W. Morrison, M. Flannery, At. Data Nucl. Data Tables **16**, 495 (1975)
15. J. Hirschfelder, C. Curtis, R. Bird, *Molecular Theory of Gases and Liquids* (Wiley, New York, 1964)
16. E. McDaniel, E. Mason, *The Mobility and Diffusion of Ions in Gases* (John Wiley & Sons, New York, London, Sydney, Toronto, 1973)
17. A. Dalgarno, Adv. Chem. Phys. **12**, 143 (1967)
18. A.A. Buchachenko, G. Chałasiński, M.M. Szczęśniak, Eur. Phys. J. D **45**, 147 (2007)
19. R. Lide, *CRC Handbook of Chemistry and Physics*, 74th edn. (CRC Press, Boca Raton, 1993)
20. J. Kirkwood, Z. Phys. **33**, 57 (1932)
21. B. Gray, E. Lee, A. Yousef, S. Shrestha, L. Viehland, T. Wright, Mol. Phys. **104**, 3237 (2006)
22. S. Hofmann, G. Münzenberg, Rev. Mod. Phys. **72**, 733 (2000)
23. C. Düllmann, Eur. Phys. J. D **45**, 75 (2007)
24. H. Backe, P. Kunz, W. Lauth, A. Dretzke, R. Horn, T. Kolb, M. Laatiaoui, M. Sewtz, D. Ackermann, M. Block, F. Herfurth, F.P. Heßberger, S. Hofmann, R. Mann, Eur. Phys. J. D **45**, 99 (2007)
25. D. Dahl, *SIMION 3D 7.0* (Idaho National Engineering Laboratory, 2000)
26. M.A. Hassouba, F. Elakshar, A. Garamoon, Fizika A **11**, 81 (2002)
27. J. Neumayr, P. Thirolf, D. Habs, S. Heinz, V. Kolhinen, M. Sewtz, J. Szerypo, Rev. Sci. Instrum. **77**, 065109 (2006)
28. Fluent Inc., *FLUENT 6.2 User's Guide* (Fluent Inc., Lebanon NH 03766 USA, 2005)
29. L. Viehland, E. Mason, Mol. Phys. **47**, 709 (1982)
30. M. Guest, A. Ding, J. Karlau, J. Weise, L. Hillier, Mol. Phys. **38**, 1427 (1979)